9-1-2014

Passive Rotation Joint Design Considerations for Lift and Thrust Generation for a Biomimetic Flapping Wing

Garrison J. Lindholm

Richard G. Cobb
Air Force Institute of Technology

Recommended Citation

Lindholm, G. J., & Cobb, R. G. (2014). Passive Rotation Joint Design Considerations for Lift and Thrust Generation for a Biomimetic Flapping Wing. International Journal of Micro Air Vehicles, 6(3), 141–154. https://doi.org/10.1260/1756-8293.6.3.141

Passive Rotation Joint Design Considerations for Lift and Thrust Generation for a Biomimetic Flapping Wing

Garrison J. Lindholm and Richard G. Cobb
Air Force Institute of Technology, WPAFB, OH, 45433

ABSTRACT

Maximizing the available lift and thrust force is important for designing efficient flapping wing micro air vehicles. Research to date showed the passive rotation joint between the wing and four-bar linkage is an important design aspect. Two key hinge parameters are the angle of attack stop and passive rotation joint stiffness. In this work these design parameters were independently varied. Their impact on lift and thrust force generation, and the ratio of the first and second system resonance frequencies were measured and compared through experiments utilizing prototype hardware of varying design. The prototype hardware and flapping wing controller is based on previous work, focused on using biomimetic wings combined with a design that only requires two piezoelectric actuators, and will be briefly reviewed. The angle of attack stops tested were 30˚, 40˚, 45˚, 50˚, and 60˚. Five different passive rotation joints were tested of varying stiffness. Optimal angle of attack stops and passive rotation joint designs were found from the experimental results and combined into a best design, which was tested and compared to the optimal results from the independent designs. Results show that while individual selection of angle stop and passive rotation joint stiffness can be optimized, the intersection between the two precludes simply choosing the best of both as the best combined.

NOMENCLATURE

A	Stroke amplitude
AFIT	Air Force Institute of Technology
BABM	Bi-harmonic Amplitude and Bias Modulation
DHPC	Discrete Harmonic Plant Compensation
DOF	Degrees of Freedom
ERA	Eigensystem Realization Algorithm
FRF	Frequency Response Function
FWMAV	Flapping Wing Micro Air Vehicle
L	Length
M	Harmonic coefficient
W	Width
X^B	Force in the x-body direction
Y^B	Force in the y-body direction
Z^B	Force in the z-body direction
t	Thickness
α	Angle of attack
β	Harmonic phase shift
κ	Stiffness
η	Wing stroke bias
θ	Elevation angle
τ	Split-cycle parameter

ϕ	Stroke angle or phase angle
ω	Flapping frequency

Subscript

c	Carbon fiber
h	Passive rotation joint hinge
m	Maximum value
n	Natural frequency
p	Predicted
s	Angle of attack stop
L	Left wing
R	Right wing
1	First resonant mode
2	Second resonant mode

1. BACKGROUND

The Air Force Institute of Technology's (AFIT) flapping wing micro air vehicle (FWMAV) research program is focused on creating a minimally actuated, power tethered, bio-mimetic flight test vehicle. Current designs utilize two, single degree of freedom piezoelectric actuators to provide control of five of the FWMAV's six degrees of freedom (DOF).

The simplified design requires only two drive signals, $\phi_L(t)$ and $\phi_R(t)$ for control. A prescriptive method is used to generate these drive signals in an open loop, requiring no feedback of wing dynamics. [1, 2] Previous work has developed a wing that mimics the structural dynamics of the *Manduca sexta*. [3, 4] Developed FWMAV production techniques have created FWMAVs that generate useful forces and moments, but have yet to achieve a lift to weight ratio greater than one. [5, 1] Research to date showed the passive rotation joint between the wing and four-bar linkage is an important design aspect. Two key joint parameters are the angle of attack stop, α_s, and passive rotation joint stiffness, κ_h, with the assumption that α_s holds the wing at this angle through a wing stroke half-cycle, and κ_h determines the ratio of the system second resonant frequency to the first resonant frequency, ω_{n2}/ω_{n1}.

Based on previous results, additional work is required to reduce weight and increase lift and thrust forces to achieve the goal of controlled flight. [2, 3] By testing prototype devices in a series of designs varying α_s and κ_h independently, available lift and thrust will be optimized, while maintaining acceptable ω_{n2}/ω_{n1}. ω_{n2}/ω_{n1} is an important parameter, as previous results have indicated that an ω_{n2}/ω_{n1} near 2 will reduce thrust production by violating the assumption that the wing is held at α_s through a wing stroke half-cycle due to the rotation joint being over excited by the second harmonic term in the wing stroke function eqn (2).

Previous work with different wing shape and sizes have shown experimentally and analytically that α_s and κ_h influence aerodynamic force production. Dickinson measured the instantaneous forces in the upstroke and downstroke of an dynamically scaled insect wing. [6] Clear peaks in lift and drag were found for an angle of attack of approximately 45°. Combined with results in [7], it was concluded that the timing and speed of the wing rotation at the end of each stroke significantly impacted the force production.

Whitey and Wood investigated the concept of a passive rotation of the wing in insect and FWMAV flight, finding that the passive rotation dynamics has significant impact in force production.[8] Experiments were performed and a blade-element model was developed predicting forces and the passive rotation joint trajectory. In [9] many configurations of a hummingbird sized FWMAV were tested. Variations were made in wing geometry and angle of attack, and showed very distinct maximums in lift production for these design parameters. Specifically for their hummingbird sized FWMAV, 12.5° angle of attack was found to maximize lift force production at 8 grams.

Byl developed a model and used it to examine the effect of angle of attack and wing rotation stiffness on force production for a hummingbird and fly sized FWMAV.[10] Both the angle of attack, as well as the wing rotation stiffness, had a major impact on force production. For example, when using a 45° angle of attack, the optimal rotation stiffness generated 93% of the optimal predicted force. Whereas non-optimal rotation stiffness resulted in as low as 20% of the optimal predicted force.

The literature documents the significant changes in force production due to wing rotation angle and rate, but does not provide design tools for use during mechanism design and construction. In this work,

the two components of the FWMAV passive rotation joint, α_s and κ_h, are examined for the impact they have on force production. It is expected that for each parameter there will be an optimal value for force production.

The relationship between the two parameters will not be explored; instead, each parameter will be considered independent of the other. The assumption is that optimizing each component separately will produce an optimal design when combined in a final flapping mechanism. This assumption will be challenged by testing a final design combining the optimal results of the two independent studies.

1.1 Vehicle Controller

In order to understand how the FWMAV's actuators will be driven, the control scheme used will be reviewed. The FWMAV control scheme used to drive the piezoelectric actuator is called Bi-harmonic amplitude and bias modulation (BABM). The scheme was proposed and evaluated previously, [11, 1] and is presented in a summary form here so the control parameters are well understood.

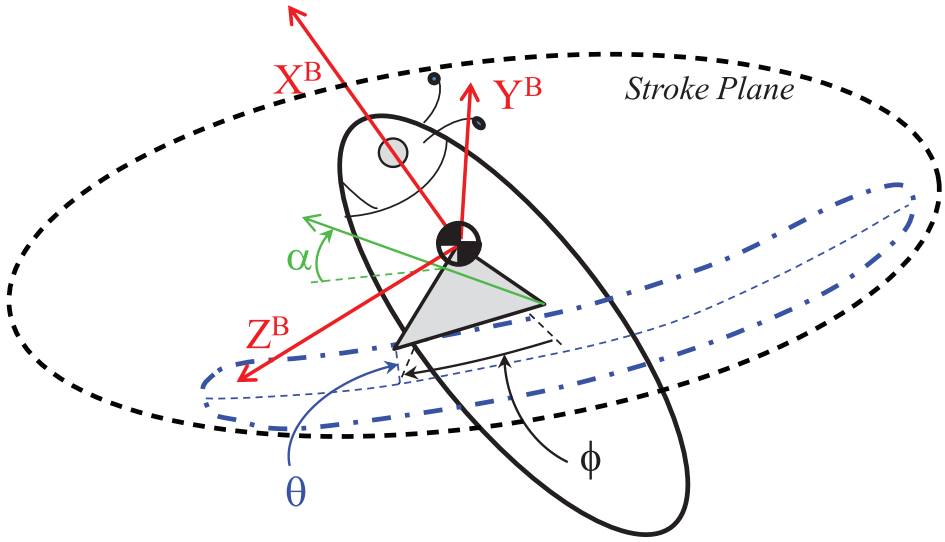

Figure 1. FWMAV coordinate frame definitions.[1]

Consider figure 1, which defines the FWMAV wing kinematics and body-fixed coordinate frame. Three angles define the position of the wing at any point in a stroke cycle: ϕ, stroke angle, θ, elevation angle, and α, angle of attack. For the BABM controller, the elevation angle is fixed and the angle of attack is controlled by an angle limited passive rotation joint, that is assumed to be constant during the up and down half-stroke cycles. This assumption is an approximation to the true motion which has been measured experimentally, as shown in [12], and modeled in [8], however keeping this constant assumption prevents predictions and data analysis from becoming intractable. In addition, the cycle-averaged forces are the main concern, as opposed to the inter-cycle forces. Therefore, for BABM control only the stroke angle of each wing is modified. The stroke angle function is controlled through three control parameters; amplitude, split-cycle parameter, and bias that directly influence the motion of the FWMAV, thereby allowing for full control of the vehicle. The split-cycle parameter creates a wing trajectory where the upstroke and downstroke are asymmetric, shifted approximately by $\pm\tau$, as shown in figure 2. This asymmetric waveform creates a non-zero net drag force over the cycle of the flapping wing, while only marginally decreasing lift, and is used in the control of the FWMAV. [8, 2] It is desirable maximize this net drag force per value of τ for a given FWMAV. The term $\partial T/\partial\tau$ will be used to represent the amount of net drag force or thrust, produced per τ used. For simplicity, eqn (1) shows the split-cycle stroke angle function without the amplitude or bias parameters,

$$\phi(t) = \begin{cases} \cos[\omega(1-\Delta)t] & \text{for} \quad 0 \le t \le \frac{\pi}{\omega(1-\Delta)} \\ \cos[\omega(1+\Sigma)t + \xi] & \text{for} \quad \frac{\pi}{\omega(1-\Delta)} < t \le \frac{2\pi}{\omega} \end{cases} \tag{1}$$

where, $\Sigma = \frac{\Delta}{1-2\Delta}$, $\xi = \frac{-2\pi\Delta}{1-2\Delta}$, and $\Delta = \frac{2\tau}{1+2\tau}$ thereby making the split-cycle stroke angle function in terms of τ, split-cycle parameter, and ω, flapping frequency.

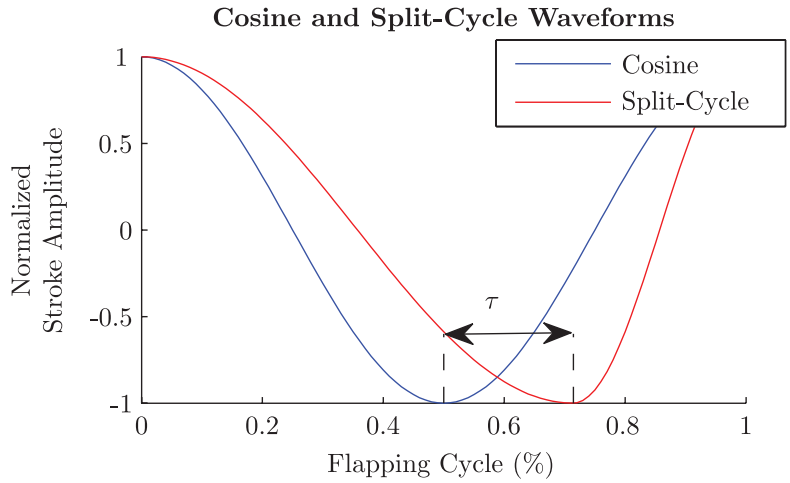

Figure 2. Idealized split-cycle wing trajectory.

In practice however, it was found that the FWMAV wings did not adequately track the split-cycle waveform while flapping at the mechanism's first resonant frequency, but a truncated Fourier sum approximation of eqn (1) of the trajectory could be tracked by using a discrete harmonic plant compensation (DHPC) technique. Using DHPC the stroke angle function can be approximated to the following stroke angle function. The addition of an amplitude and bias term completes the BABM stroke angle function. The control parameters in the stroke angle function can then be applied symmetrically to both wings or asymmetrically as needed in order to obtain the desired control response. Using this method of control, it has been shown that five of the DOF can be controlled, thus allowing sufficient control over the vehicle for flight. [1] As implemented, the DHPC-BABM control is given as:

$$\phi(t) = A\{M_1(\tau)\cos[\omega t + \beta(\tau)] - M_2(\tau)\sin[2\omega t + 2\beta(\tau)]\} + \eta \tag{2}$$

where ω is the flapping frequency and the three control parameters are: A, stroke amplitude, τ, split-cycle parameter, and η, stroke bias and M_1, M_2, and, β are harmonic coefficients and phase shifts that are functions of τ defined as:

$$M_1(\tau) = \frac{\cos(2\tau)}{M_{\omega_n}} \tag{3}$$

$$M_2(\tau) = \frac{0.34\sin(3.3\tau)}{M_{2\omega_n}} \tag{4}$$

$$\beta(\tau) = -2\tau - \phi_{\omega_n} \tag{5}$$

where $M_{\omega n}$ is the magnitude of the wing displacement at the first system resonance as measured by a

frequency response function (FRF), $M_{2\omega n}$ is the magnitude of the wing displacement at twice the first system resonance, and $\phi_{\omega n}$ is the phase of the wing displacement at the first system resonance. It is undesirable to have the system's second resonant frequency at $2\omega_n$, as this tends to over-excite the passive rotation joint and prevents the angle of attack from remaining relatively constant through the stroke half-cycle, as was assumed in the BABM control formulation. This motivated the use of the joint stiffness, κ_h, as a means to move the second resonant frequency away from $2\omega_n$. The FRF was found by measuring the actuator tip displacement as the output while a low amplitude swept sine wave drive signal was used as the input. The FRF of the flapper was then modeled using an eigensystem realization algorithm (ERA) as a four state, discrete state-space model to extract parameters of $M_{\omega n}$, $M_{2\omega n}$, and $\phi_{\omega n}$. [13, 14]

In this bench level work, a single wing flapper was used, hence there is only one stroke angle function. Amplitude and the split-cycle parameters were varied in the testing, but the bias was left unchanged for all tests. Ideally, the bias does not effect lift and thrust and is only used to move the center of pressure, and thus produce a moment in dual wing systems.

2. EXPERIMENT SETUP

This work was performed utilizing a single-actuator, single wing flapper mechanism, rather than a multiactuator and wing FWMAV. The single wing flapper is dynamically identical to the full dual-wing FWMAV, but does not include the complexity required for lightweight flight models. In this work the single wing flapper was used in two distinctly different test suites. The first tests varied one component of the flapper, α_s, while leaving all the other design variables fixed. The second tests were performed with a fixed α_s while varying the κ_h parameter. Finally the optimal from both will be combined as a final design.

2.1 Single Wing Flapper Mechanism Design

The single wing flapper is shown in figure 3. It consists of the following components: wing, passive rotation joint, angle of attack stops, 4-bar linkage, piezoelectric actuator, carbon fiber frame, and rapid

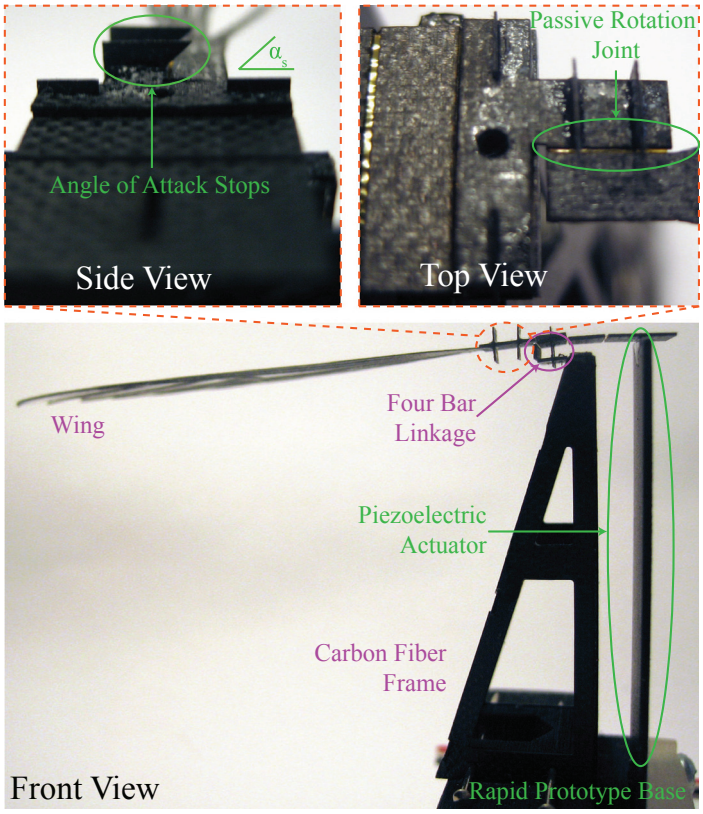

Figure 3. Side, top, and front view of single wing flapper used in this study with individual components labeled.

prototype base. The wing was designed to mimic the structural dynamics of a $M.\ sexta$, as reported in [3, 4]. The 4-bar linkage is designed to create a $\pm 55^{\circ}$ stroke angle to match the $M.\ sexta$. The bimorph piezoelectric actuator used was an Omega Piezo Technologies Inc. OPT 60/20/0.6 and provides an input deflection to the linkage and thus drives the wing. The actuator can be driven at variable amplitude, waveform shapes, and flapping frequencies. The carbon fiber frame and rapid prototype base provide stiff boundary conditions for the actuator and linkage, and also provide a mounting point to a force balance. In this study α_s and κ_h will be varied in order to capture their effect on lift and thrust force production.

2.1.1 Angle of Attack Stops

The angle of attack stops were initially set at 45° and, using the same design used in previous studies. [3] Additional angle of attack stops were designed as seen in figure 4. Angle of attack stops of 30°, 40°, 45°, 50°, and 60° were designed, produced, and tested. The angle of attack stops are required to prevent the wing from over rotation during flapping, but do not guarantee that this angle is held constant during each stroke half-cycle.

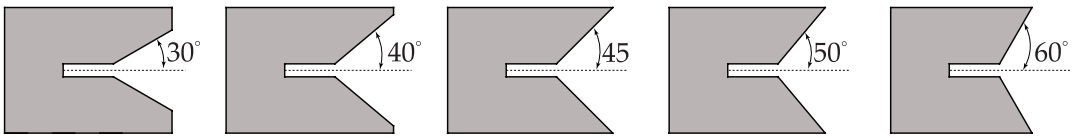

Figure 4. Side view of angle of attack stops.

2.1.2 Passive Rotation Joint Stiffness

In addition to the angle of attack stops, the stiffness of the passive rotation joint was varied, and its impact on the first and second resonant frequencies or modes were measured. The first resonant mode of the single wing flapper is the wing stroke angle. The second resonant mode is the rotation of the wing around the passive rotation joint. It is assumed that by changing the stiffness of the passive rotation joint the frequency of the second resonant mode can be changed as desired. The motivation for this study was due to the original passive rotation joint design consistently resulting in the second resonant mode at twice the first resonant mode. This is not desirable as twice the first resonant mode is used in the second harmonic term in the BABM control signal to generate the split-cycle waveform using $M_{2\omega n}$ from eqns (2) and (4). Therefor, when the second resonant mode is twice the first resonant mode, the passive rotation joint was being over-excited giving an undesirable rotation of the wing, thus preventing the angle of attack from remaining relatively constant during the half-stroke cycle as was previously assumed.

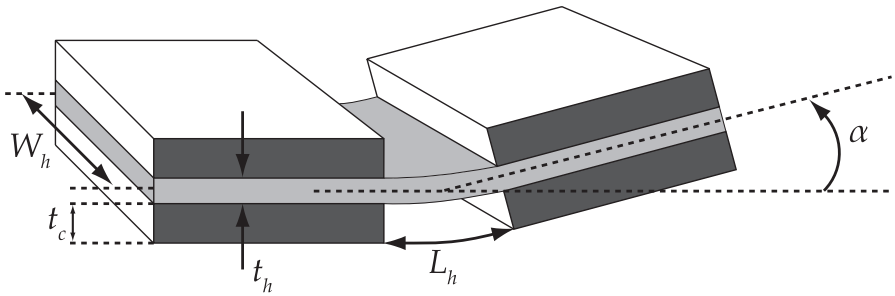

Figure 5. Geometry of the passive rotation joint design.

Lift and thrust production were also measured in order to see the passive rotation joint stiffness impact on force production. The hinge of the passive rotation joint can be changed by adjusting the geometry, as seen in figure 5, or by using different materials for the hinge. The passive rotation joint's rotational stiffness can be modeled as a linear elastic beam deforming under an external moment:

$$\kappa_h = \frac{E_h t_h^3 W_h}{12 L_h} \tag{6}$$

where, t_h, W_h, and L_h are the thickness, width, and length of the hinge layer, t_c, is the thickness of the carbon layer above or below the flexure layer, and E_h is the modulus of the hinge material. [8] Additionally, the predicted max deflection of the rotation joint can be computed:

$$\alpha_{mp} = \frac{\pi}{2} - \frac{L_h}{t_c} \tag{7}$$

Table 1. Tested design hinge stiffness, length, and maximum rotation angles.

Design	κ_h **Predicted (n-m/rad)**	α_m **Predicted (deg)**	**Hinge Length (mm)**
Original	6.22E-5	95.5	0.2500
x1.25	7.78E-5	76.1	0.1992
x1.5	9.36E-5	63.1	0.1651
x2.0	1.24E-4	47.7	0.1250
x2.5	1.56E-4	38.2	0.1000
x3.0	1.87E-4	31.8	0.0833

where α_{mp} was the predicted maximum rotation angle. The angle of attack stops are used to prevent the rotation of the wing from exceeding the maximum rotation angle. In this study the material, thickness, and width of the rotation joint are left fixed, and the length of the hinge was varied. The hinge material used was 25 micron Kapton and the designed hinge width was 4.78 mm. Table 1 shows the tested hinge stiffness, designed hinge length, and predicted maximum rotation angle. Designed hinge length differs from the actual hinge length due to the additional material removed in the laser micromachining process used to manufacture the flapping mechanism. The differing length of the designed versus manufactured hinges also impacts the actual maximum rotation angle versus the designed maximum rotation angle.

2.2 Testing Procedure

The test setup is similar to one used previously with the addition of a force balance. [15] A MATLAB script was used to generate the voltage profile, which was then sent to the power amplifier through a National Instrument's USB-6229 BNC ADC/DAC box, which has a ± 10 volt output range. Using this script, the flapper can be driven at any desired flapping frequency. A Trek PZD700 amplifier was used to amplify the drive signal x30 to drive the bimorph piezoelectric actuator. Cycle-averaged lift was measured using an ATI Industrial Automation Nano 17 Titanium 6 axis force balance, which has a force resolution of 1/682 N resolution and up to a 14.1 N range. Figure 6 shows a diagram of the experiment setup.

For each design under test, an FRF was found for the flapping mechanism by using a low amplitude swept sine signal as the input, and a laser displacement sensor focused on the tip of the actuator as the output. The FRF measures key values used in the controller in eqns (3) to (5), specifically $M_{\omega n}$, $M_{2\omega n}$, and $\phi_{\omega n}$, as well as the resonant frequencies of the first and second modes of the flapping mechanism.

With the controller parameters measured, data points were collected for each given design, using the following signal parameters: flapping frequency equal to the first mode, amplitude fixed, and split-cycle parameter varied for each test point. Each test consisted of 100 cycles of flapping. Measurements were taken in the middle of the test period while the flapper was in a steady-state flapping motion. Each test was repeated 5 times to get mean and standard deviation data for the given design.

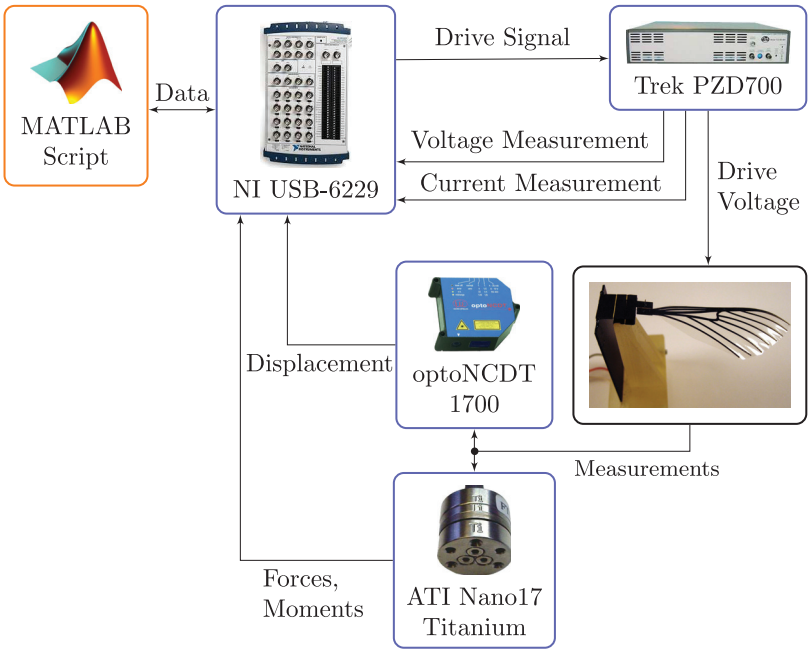

Figure 6. Diagram of experiment setup.

3. RESULTS

In this section the results, of varying α_s and κ_h, will be presented. To help identify outliers and recognize trends in the measured data, an additional data set generated from a blade element model presented in [16], using the model's parameters for the flapper and each test condition, was added.

3.1 Angle of Attack Stops

In figure 7, it is seen that the experimental results outperformed the blade element model consistently. This is expected from previous results [16], however the trend in the data matches, with the exception

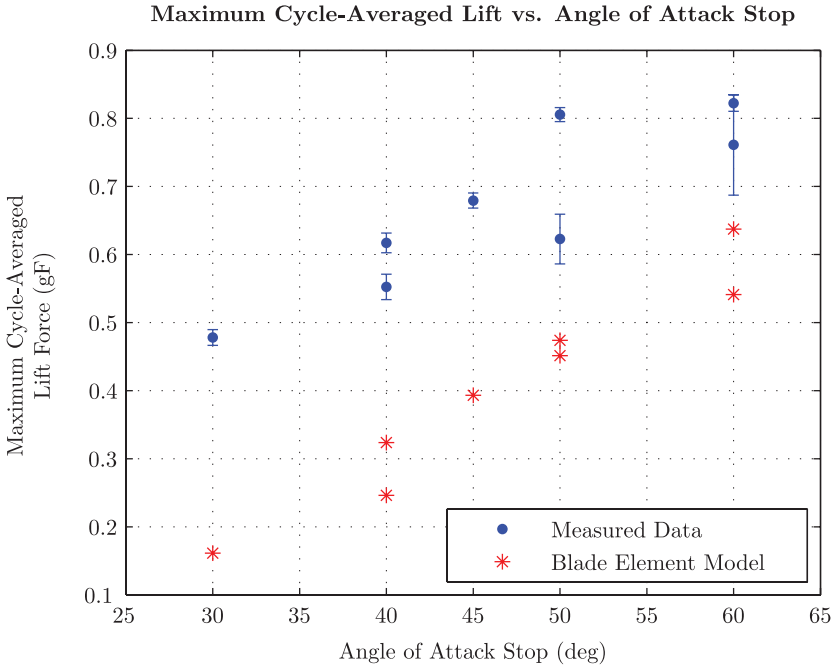

Figure 7. Lift versus angle of attack stop angle, repeat test points are for different test mechanisms operating at different flapping frequencies. Error bars represent one σ.

of the data in the 50-60 degree range. Here, the blade element model shows increasing lift with increasing angle of attack, however the experimental data shows no increase in lift. This is likely due to the wing beginning to stall for this range of angle of attack, which the equation for lift coefficient in the blade-element model did not predict. From this data, in order to maximize lift, flapping mechanisms using this wing should use an angle of attack stop in the 50-60 degree range.

Next, data was measured for each α_s design as the split-cycle parameters -0.05, -0.025, 0, 0.025, and 0.05 were tested, while amplitude was held fixed at 0.4. The cycle-averaged thrust, T, was then plotted versus the split-cycle parameter, τ, for each α_s design. A linear fit was applied to each plot and the slope was recorded as $\partial T/\partial\tau$. The results for each α_s design are shown below in figure 8. A higher magnitude of $\partial T/\partial\tau$ is desirable as it represents more control authority while using the split-cycle waveform, and blade-element theory predicts the slope should be negative. As can be seen, with small α_s, there is a large magnitude but opposite sign of what was expected from blade-element theory. This is likely due to asymmetric inertial forces being larger than asymmetric aerodynamic forces when using the smaller amplitude angle of attack stops. Then, as the α_s is increased $\partial T/\partial\tau$ returns to the expected negative values. Also it is seen that the magnitude increases as α_s increases.

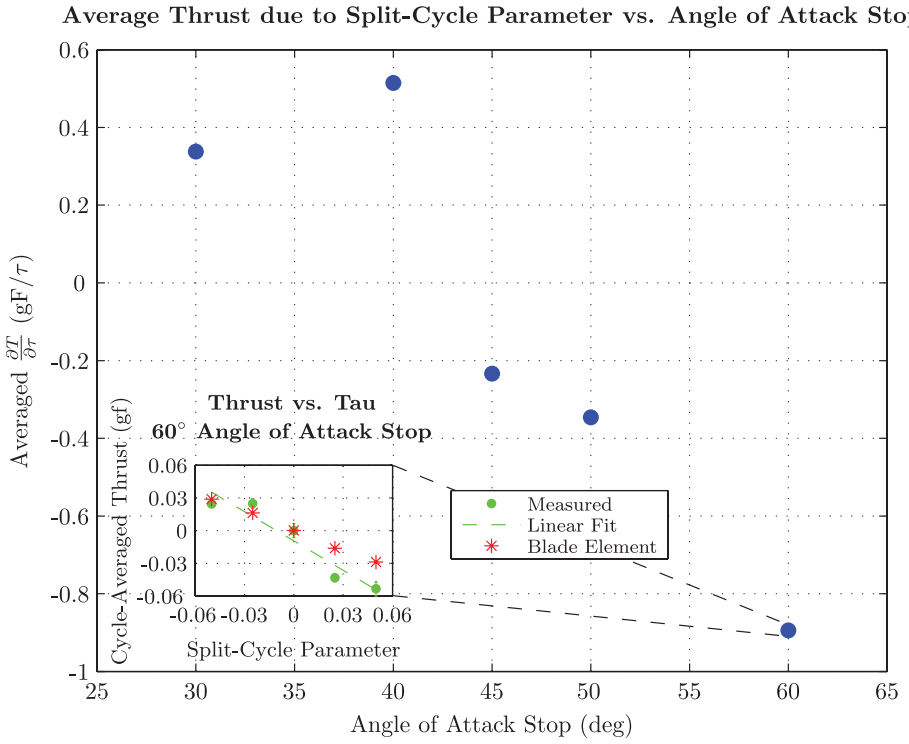

Figure 8. Main figure, thrust generation per split-cycle parameter as the angle of attack stops were varied. Inset figure, measured, linear fit, and blade element data points used to calculate the thrust per split-cycle for 60 degree angle of attack stop.

Reviewing the previous lift and thrust results, the most desirable α_s design appears to be 60 degrees. This α_s demonstrated the maximum lift values, and also had the highest magnitude $\partial T/\partial\tau$ with the correct sign.

3.2 Passive Rotation Joint Stiffness

Multiple flappers for each design in table 1 were built and the measured frequency response data were averaged to reduce the impact of manufacturing variation on the results. Figure 9 shows measured and modeled FRFs of two different κ_h designs. The dominant first and second resonant frequencies of each design can clearly be seen.

Table 2 shows the first and second resonant modal frequencies, damping ratios, and the ratio of the

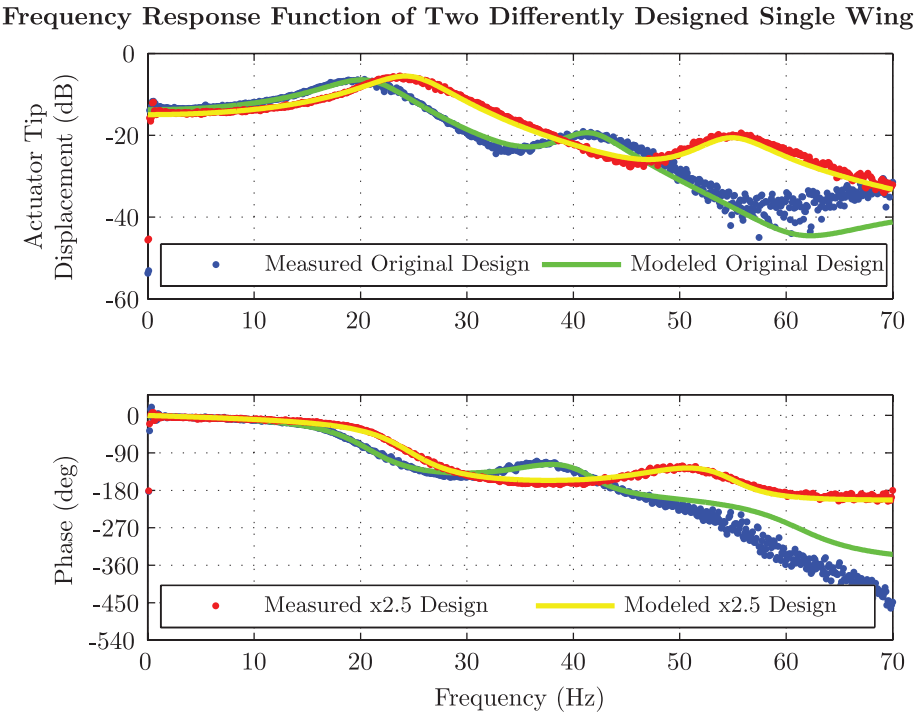

Figure 9. Example measured and modeled single wing flapper frequency response function for the original and x2.5 passive rotation joint designs.

second resonant mode to the first resonant mode for each κ_h design. It can be seen that at and near the original stiffness, ω_{n2}/ω_{n1} is near 2. This behavior was previously explained to be detrimental for use with BABM control scheme. As κ_h increases, an increase in this ratio is seen, which moves the second mode away from twice the first mode frequency. This demonstrates that κ_h is a useful tool in the FWMAV designer's toolbox for adjusting the ratio of these frequencies as desired. It is also seen that in the x2.5 and x3 range there is an increase in the first resonant flapping frequency, this correlates to the higher lifting forces seen in figure 10, as lift is proportional to the square of the flapping frequency. However, in the case of the x3 design, it is seen that the damping ratio is much higher for the first mode when compared to all other designs. This may be a sign that the joint is too stiff in this case and may not allow the desired passive rotation of the wing(desired rotation is to rotate wing until it hits the angle stop) and correlates to the lower measured lift values seen in figure 10.

Figure 10 shows the measured lift force as κ_h was changed. Strange behavior was noted as the maximum lift generated alternates high and low between designs. This effect is not well understood as multiple mechanisms were tested for each joint design and the results were repeatable. The cause of this phenomenon could be due to the angle of attack stops not being adequate enough to set a specific angle of attack along the span of the wing, as there is significant flexibility built into the wing. However, as expected from table 2, the maximum lift was found for the higher flapping frequency x2.5 design and the x3 design maximum lift drops off dramatically. It seems clear that the passive rotation joint stiffness plays a role in maximum cycle-averaged lift, but there appears to be more complex

Table 2. Averaged first and second modal results due to changing passive rotation joint stiffness.

	Mode 1		Mode 2		$\frac{\omega_{n2}}{\omega_{n1}}$
Design	ω_n **(Hz)**	ζ **(%)**	ω_n **(Hz)**	ζ **(%)**	
Original	21.12	18.35	41.55	7.35	1.97
x1.25	22.48	14.93	46.55	6.76	2.07
x1.5	22.78	15.49	46.73	8.25	2.05
x2	21.32	16.05	48.03	6.67	2.25
x2.5	25.29	15.10	56.56	6.92	2.24
x3	25.64	23.17	59.89	6.89	2.34

interactions then the single varied parameter causing the alternating behavior as shown. Also, this alternating behavior limits the effectiveness of an independent two parameters optimization.

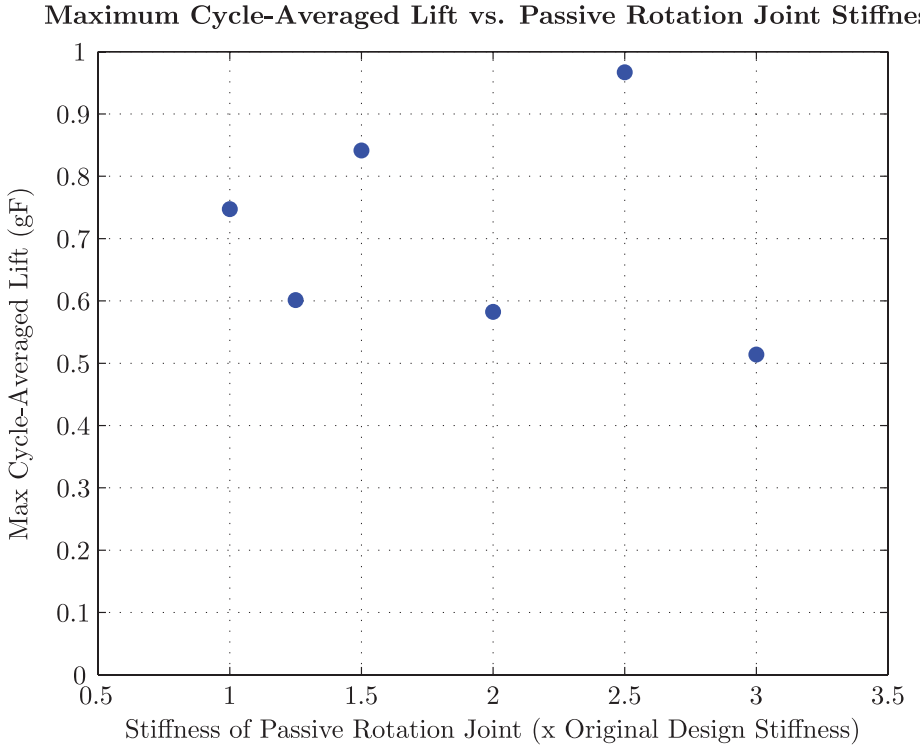

Figure 10. Maximum measured cycle-averaged lift for varying passive rotation joint stiffness.

Next, data was measured for each κ_h design as the split-cycle parameters were varied using the same input parameters that were used for the varying angle of attack stop tests. The cycle-averaged thrust was plotted versus the split-cycle parameter for each passive rotation joint design. A linear curve fit was applied to each plot and the slope was recorded as $\partial T/\partial\tau$. The results for each passive rotation joint design are shown in figure 11. As already mentioned, a higher magnitude of $\partial T/\partial\tau$ is desirable as it represents more control authority when using the split-cycle waveform. As can be seen, there is a trend that as the passive rotation joint is made stiffer, $\partial T/\partial\tau$ increases in magnitude up until the x2.5 design then the trend reverses with the stiffest design. The initial trend was expected from the modal frequencies, examined earlier, predicted less excitation of the second rotational mode as the stiffness was increased, the reversal of the trend was not predicted and is likely caused by the rotation of the wing being either too slow or late in the stroke cycle. Reviewing the results of the modal analysis, lift force, and thrust force, the most desirable passive rotation joint stiffness is the x2.5 design. This joint stiffness corresponded to the maximum lift, maximum $\partial T/\partial\tau$, and moved the ratio of the second mode to the first mode frequencies away from the original value of 2.

3.3 Combined Test

The optimal results from the two separate parameter design studies, 60° α_s and the x2.5 κ_h design, were then combined in a single mechanism. This single wing flapper produced an average of 0.63 gF of lift, -0.20 $\partial T/\partial\tau$ and the ratio of the first resonant mode to the second resonant mode was 2.4.

Table 3 compares the results of the independent parameter designs with the combined results and demonstrates that the optimization of these hinge parameters separately and then combining the results into a unified design did not produce an optimized hinge design for a given wing. An optimization process should be used that varies the two parameters together, while still minimizing the total number of prototypes and testing that need be accomplished.

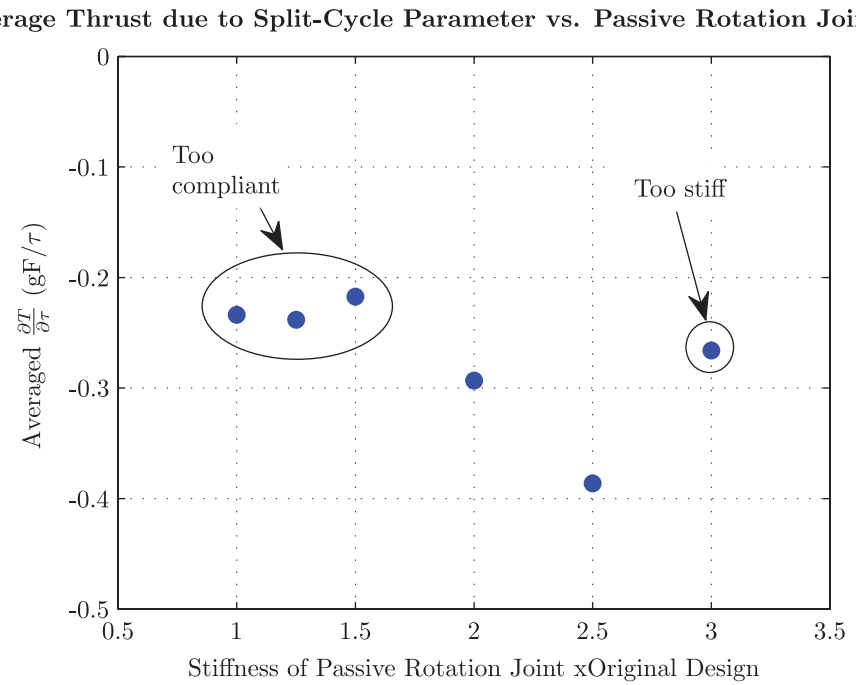

Figure 11. Thrust generation per split-cycle parameter as the passive rotation joint stiffness were varied.

Table 3. Experimental results of optimal α_s, κ_h and combined designs for lift and thrust production and ω_{n2}/ω_{n1}.

α_s **Design**	**60°**	**45°**	**60°**
κ_h **Design**	**Original**	**x2.5**	**x2.5**
Lift (gF)	0.79	0.97	0.63
$\partial T/\partial \tau$	−0.89	−0.39	−0.20
ω_{n2}/ω_{n1}	1.9	2.2	2.4

4. CONCLUSION

In this work, a simplified two parameter design space was used to optimize a biomimetic FWMAV for maximum lift and thrust production, as well as tailoring the ratio of the first and second resonance modes.

First, the effect of α_s on lift and thrust force generation while using the BABM control method was explored. It was found that larger α_s correlated with higher values of lift and thrust. An ideal α_s was found to be 60 degrees. Future work could be done to explore optimal α_s as a function of flight velocity and angles further refined from the values tested here.

The other design parameter tested was κ_h. It was anticipated that tracking and tuning the modal frequencies via κ_h, as measured on the drive actuator would be a sufficient indicator to optimize force generation, however this technique was experimentally demonstrated to be insufficient. κ_h was found to influence the ratio of the second mode to the first mode frequencies. It also had a minor effect on the value of the the first flapping frequency. It was shown that stiffer κ_h increased lift generation in an alternating pattern. This alternating pattern could not be explained currently but could it is conjectured that additional flexibility in the wing structure precludes this simplified approach. Potential future work to provide insight into this effect could be done using high-speed video, particle image velocimetry, or complex fluid/structural computational dynamic studies to understand the differences in the flow field structure with the different κ_h values. Also, increasing the stiffness tended to increase thrust generation up to an optimal stiffness. The optimal joint stiffness design was found to be 2.5 times stiffer than the original design. Without further work in optimizing κ_h, the dual-piezo driven FWMAV is still possible, but will not operate with maximum power efficiency.

Last, the two optimal parameters were combined into a single design. The resulting design was then tested and compared to the individual design studies. The result showed that the approach of optimizing the design, by doing two separate independent design studies and then combining the results, was not a valid technique. Future work on κ_h is needed to optimize the FWMAV to maximize lift and thrust production while maintaining an acceptable ratio of the first and second resonance modes.

ACKNOWLEDGMENTS

This work was funded by the Air Force Research Laboratory, Air Vehicles Directorate under the direction of Dr. Gregory Parker. The views expressed in this article are those of the authors and do not reflect the official policy or position of the United States Air Force, Department of Defense, or the U.S. Government.

REFERENCES

[1] M. L. Anderson, N. J. Sladek, and R. G. Cobb, "Evaluation of bi-harmonic amplitude and bias modulation for flapping wing MAV control," *Proceedings from the 49th AIAA Aerospace Sciences Meeting including the New Horizons Forum and Aerospace Exposition*, 1/4 2011.

[2] M. L. Anderson and R. G. Cobb, "Toward flapping wing control of micro air vehicles," *Journal of guidance, control, and dynamics*, vol. 35, no. 1, pp. 296–308, 2012.

[3] R. P. O'Hara, "The material property and structural dynamic characterization of the Manduca Sexta forewing for application to flapping micro air vehicle design," *Dissertation, Air Force Institute of Technology*, 2011.

[4] R. O'Hara, N. DeLeón, and A. Palazotto, "Structural identification and simulation of the Manduca Sexta forewing," *Proceedings of the 2011 AIAA Conference on Structures, Structural Dynamics, and Materials*, 2011.

[5] M. L. Anderson, R. P. O'Hara, and R. G. Cobb, "Design, fabrication, and testing of an insect-sized MAV wing flapping mechanism," *Proceedings from the 49th AIAA Aerospace Sciences Meeting*, 1/4 2011.

[6] M. Dickinson, "The effects of wing rotation on unsteady aerodynamic performance at low Reynolds numbers," *Journal of experimental biology*, vol. 192, no. 1, pp. 179–206, 1994.

[7] C. P. Ellington, "The aerodynamics of hovering insect flight. IV. Aerodynamic mechanisms," *Philosophical Transactions of the Royal Society of London. B, Biological Sciences*, vol. 305, no. 1122, pp. 79–113, 1984.

[8] J. P. Whitney and R. J. Wood, "Aeromechanics of passive rotation in flapping flight," *Journal of Fluid Mechanics*, vol. 660, no. 1, pp. 197–220, 2010.

[9] A. Yilmaz, "Design and development of a flapping wing micro air vehicle," *Swiss Federal Institute of Technology Zurich, Autonomous Systems Lab*, 2010.

[10] K. Byl, "A passive dynamic approach for flapping-wing micro-aerial vehicle control," *ASME Dynamic Systems and Control Conference, Cambridge, Massachusetts, USA*, pp. 13–15, 2010.

[11] M. L. Anderson and R. G. Cobb, "Techniques for non-harmonic wing flapping for the control of micro air vehicles," *Proceedings from the AIAA Guidance, Navigation, and Control Conference*, 8/2 2010.

[12] A. M. DeLuca, "Aerodynamic performance and particle image velocimetery of piezo actuated biomimetic Manduca Sexta engineered wings towards the design and application of a flapping wing flight vehicle," Dissertation, *Air Force Institute of Technology*, 2013.

[13] R. D. Woods, B. S. Liebst, and R. G. Cobb, "A state-space model of a large, lightly damped space structure," in *Proceedings from the AIAA Guidance, Navigation and Control Conference*, pp. 345–355, 1995.

[14] R. G. Cobb and B. S. Liebst, "Structural damage identification using assigned partial eigenstructure," *AIAA Journal*, vol. 35, no. 1, pp. 152–158, 1997.

[15] G. J. Lindholm, R. P. O'Hara, R. G. Cobb, and M. F. Reeder, "Power requirements for control of flapping wing micro air vehicle using piezoelectric actuators," *Proceedings of the 2012 AIAA Aerospace Sciences Meeting*, 2012.

[16] M. W. Oppenheimer, D. B. Doman, and D. O. Sigthorsson, "Dynamics and control of a biomimetic vehicle using biased wingbeat forcing functions: Part I-Aerodynamic model," *Proceedings of the 48th AIAA Aerospace Sciences Meeting Including the New Horizons Forum and Exposition*, 2010.